CHARACTERISATION OF BRIDGING TRACTIONS IN MODE-I DELAMINATION USING DISTRIBUTED STRAIN MEASUREMENTS AND NUMERICAL MODELING

L. Sorensen, J. Botsis, Th. Gmür, J. Cugnoni and L. Humbert

Laboratoire de mécanique appliquée et d'analyse de fiabilité (LMAF)
Ecole polytechnique fédérale de Lausanne (EPFL), Bât. ME, Station 9
CH-1015 Lausanne, Switzerland
john.botsis@epfl.ch

ABSTRACT

Results of bridging tractions in mode I delamination on uniaxially reinforced AS4/PPS specimens are presented. Bridging tractions determined using distributed strains and an inverse-numerical technique are compared to those obtained using a method based on the experimental measurements of energy release rate and crack opening displacement. Both experiments result in similar distributions of the bridging tractions. The two types of bridging laws are implemented in a numerical model that uses cohesive elements to calculate global force-displacement response. In both cases the cohesive model can describe the global load-displacement curve well. However, the J-integral method requires an additional assumption about the length of the bridging zone. Regardless of the law used to define the bridging tractions, the cohesive model requires certain assumptions regarding the initial stiffness of the cohesive elements and the maximum stress before softening. These parameters influence crack propagation and the resulting strains.

1. INTRODUCTION

Delamination is one of the most important failure mechanisms in layered composite materials. It occurs at the free edges due to high stresses required to maintain continuity of strains. It is also found in the composite structure as a result of low impact loads, fatigue, etc. Consequently, its characterisation and prediction assume a position of prominence in the mechanics of composites. Several efforts have been devoted to studying delamination in various composite materials [1-8]. Often delamination is characterised by using linear elastic fracture mechanics, especially for pure mode loadings. In some cases, however, composites may display crack bridging (fibres crossing the open crack) which makes delamination behaviour geometry dependent [2,4,5,8] as reflected in the energy release rate (ERR) J (or G_I) versus crack opening displacement (COD) δ data. Recent studies simulate delamination propagation by using advances in interfacial cohesive element modeling [2,3,6]. Such methods have proven useful in understanding complex delamination; however, they are sensitive to the physical parameters of the process that need to be experimentally characterised. In cases of large-scale fibre bridging, some authors establish experimentally a relationship between J and δ in order to extract the traction-separation behaviour of the cohesive elements in the fibre-bridged zone [2,4]. Other investigations of delamination cracking use the spectra of optical fibre Bragg grating (FBG) sensors to measure strains near the delamination crack and attempt to correlate such data with the physical process of delamination [9-11]. Most of these studies, however, use the FBG spectrum, which alone cannot capture the location and direction of the delamination growth. Recently, a new method has been proposed to measure distributed strains over a relatively long

FBG [12]. In contrast to the T-matrix approach, no assumptions are made about the form of the axial strain distribution.

This paper focuses on analysis and comparison of data describing bridging tractions in mode I delamination determined using two different methods. The first is based on internal strain measurements taken along an embedded FBG sensor which are then applied in inverse identification algorithm to obtain the bridging tractions [5]. The second relates measurements of J (or G_I) to δ, to obtain bridging tractions. The calculated bridging tractions are compared and used in a cohesive finite element (FE) model to simulate crack growth and to predict the corresponding pin-load versus displacement curve.

2. METHODS

Unidirectional specimens are made of Cytec's AS4/PPS (carbon fibre – polyphenylene sulphide) Fiberite composite prepreg [5]. The planar dimensions of the $[0]_{28}$ plates are 200x50mm and specimens include a 60-70 mm long piece of aluminium foil treated with demoulding agent and inserted between the centre plies at one end of the specimen to create a pre-crack. In addition, an optical fibre with diameter 0.125 mm and Bragg wavelength centered at λ_B = 1300 nm is placed between the second and third layers above the centre plane and parallel to the reinforcing direction. The polyimide coating of the FBG is removed in the FBG zone plus 5 mm on both ends before being embedded. With this procedure, the FBG is located at approximately twice its diameter (i.e., twice the ply thickness or 0.264 mm) from the delamination plane. This distance is sufficiently remote from the crack to keep it from being damaged and close enough to guarantee the sensitivity of the sensor. The dimensions of the double cantilever beam (DCB) specimen are chosen according to ASTM D-5528: width = 25 mm, length = 200 mm and thickness = 3.7 mm. Specimen edges are sanded to remove imperfections that may interfere with crack growth or a clear image of the crack tip position. Afterwards steel loading blocks (25x10x10 mm) are attached to the specimen ends with 5 min (24hr cure) epoxy. Once the glue is set, correction fluid is placed along one side to provide contrast enabling the visualization of crack growth. A mechanical testing system is used to advance a mode I delamination in the specimen. In all specimens with the embedded FBG, the displacement Δ is increased at a rate of 0.01mm/min and the location of the crack tip a is continuously monitored with a digital camera and photographs are acquired manually to provide a record of the crack tip position with time. To carry out measurements using optical low coherence reflectometry (OLCR), delamination should be stationary. Thus, once its front is below the FBG sensor, the specimen is held at a constant displacement until delamination growth stops to an equilibrium position.

3. RESULTS AND DISCUSSION

3.1 Experimental

Before testing, the position of the FBG is identified by using the OLCR to measure the distance between it and the end of the optical fibre outside the specimen. Next, the specimen is loaded and delamination is followed until its front is near the FBG sensor. At this point the displacement is held constant and the FBG is interrogated. The specimen is further loaded until a longer delamination length and the measurements repeated. A typical DCB specimen with a delamination crack is shown in Figure 1 [5].

Also shown on this figure by a dotted line is the location of the optical fibre, which includes the FBG sensor. Note here the bridging fibres behind the crack tip.

.

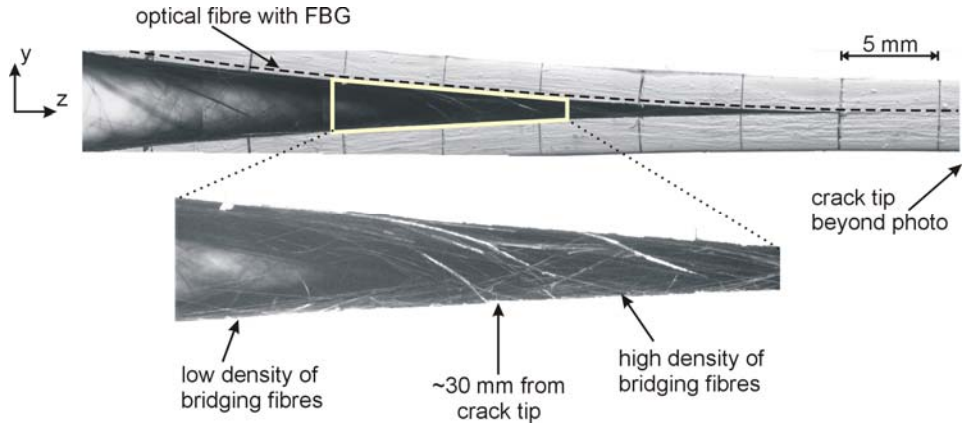

Figure 1: Photograph of a specimen with a well-developed delamination crack with bridging fibres.

In the present studies, the strain energy release rate is expressed as [13]:

$$G_I = \frac{P^2}{EIb}\left(\frac{3EI\Delta}{2P}\right)^{2/3} \qquad (1)$$

where P is the measured pin load, I is the moment of inertia of one arm, Δ is the applied displacement and b is the specimen width. For unidirectional specimens, the Young modulus is taken as $E = E_{11}$. Note that since the displacement and load data are continuously measured by the data acquisition system during testing, use of Eq. (1) reduces errors incurred when measuring crack tip position. Despite the fact that this type of simple equation neglects the effects of fibre bridging and orthotropy, it is found to give relatively good agreement with ERR calculated via FE modeling that included the effect of fibre bridging [2]. Values of G_I as a function of applied displacement tend towards a stabilization of ERR with values between 800-1100 J/m^2 which correspond well to literature data determined for carbon fibre PPS (PPS from another manufacturer) using DCB specimens (820-1350 J/m^2) [14-16]. The relatively large difference in these measurements is attributed to differences in specimens and their bridging zone sizes.

4. IDENTIFICATION OF BRIDGING TRACTIONS

4.1. Fibre Bragg grating & inverse identification of bridging tractions

It is well known that the spectral response of a homogeneous FBG in its free state (no applied strain or temperature) is a single peak centred at the Bragg wavelength λ_B as described by the Bragg condition $\lambda_B = 2n_{eff}\Lambda$, where n_{eff} is the effective refractive index for the guided mode of interest and Λ is the constant nominal period of the refractive index modulation [12]. When the FBG is embedded into a homogeneous strain field, at constant temperature, the difference in wavelength $\Delta\lambda_b$ obtained from the peak shift of the spectra, before and after loading, is related to the strain ε_z in the fibre with $\Delta\lambda_b / \lambda_B = (1 - p_e)\varepsilon_z$, where p_e is an optomechanical constant evaluated experimentally.

Spectral response, however, is significantly complicated by the introduction of non-uniform axial strains [5,12]. For example, when the FBG is near a delamination, the

spectral response becomes complicated and is sensitive to variations in the polarization state. In addition, spectral evolution lacks spatial correlation. A crack could arrive from either end of the FBG and produce the same spectral shape, indicating that the spectral form does not correspond to a unique strain state. For a constant temperature and small transverse strains so that $\varepsilon_x = \varepsilon_y \approx -\nu_f \varepsilon_z$, ($\nu_f$ is the Poisson's ratio of the optical fibre), the relationship between the non-uniform axial strains $\varepsilon_z(z)$ and the local Bragg wavelength shift $\Delta\lambda_b$ is similar to the one shown earlier, however, the $\Delta\lambda_b(z)$, $\varepsilon_z(z)$ are now dependent upon the location along the FBG:

$$\frac{\Delta\lambda_b(z)}{\lambda_B} = (1 - p_e)\,\varepsilon_z(z) \qquad (2)$$

According to (2), the axial strain distribution along the FBG can be obtained if the local wavelength evolution is known. Using an inverse scattering algorithm the local Bragg wavelength $\lambda_b(z)$ for a given polarization axis is given by [5]:

$$\lambda_b(z) = \left\{ \frac{1}{\lambda_d} + \frac{1}{4\pi n_{eff}} \cdot \frac{\mathrm{d}\phi(z)}{\mathrm{d}z} \right\}^{-1} \qquad (3)$$

where λ_d is a reference wavelength chosen within the range reflected by the FBG and ϕ is the phase of the coupling coefficient.

Wavelength shifts measured for three different delamination lengths, using an OLCR system, are given in Figure 3 [5]. Note that due to the proportionality between longitudinal strain and wavelength shift, one observes that the wavelength shifts for cracks 1, 2 and 3 are zero well ahead of the crack tip (no strain perturbation) and then rise sharply near the crack tip. Moreover, these curves can be superimposed by a simple translation, indicating a certain similarity of the field around the crack and the bridging zone.

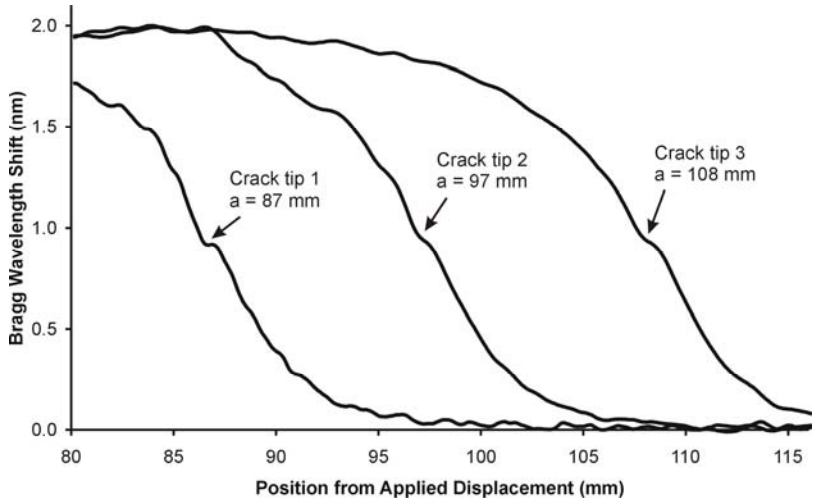

Figure 2: Measured wavelength shifts for three crack lengths. Numbers with arrows indicate crack lengths measured visually [5].

The distributed strains along the embedded FBG can be used to characterise the bridging tractions by an inverse numerical identification of a FE model including a parametric form of the bridging tractions. Details of the FE modeling are given in [5,7].

In this work, the bridging stress $\sigma_{br}(\bar{z})$ normal to the delamination plane is represented by the function:

$$\sigma_{br}(\bar{z}, \boldsymbol{\alpha}) = e^{-\bar{z}\gamma}\left(A_1 + A_2\bar{z}\right) \quad (4)$$

where $\bar{z}$ is the position from the crack tip (Figure 3) and γ is a parameter defining the degree of non-linearity of the bridging traction curve. $\boldsymbol{\alpha} = \left[\gamma, A_1, A_2\right]$ is a vector of the unknown parameters. A_1 represents the maximum stress at the crack tip $\sigma_{br\,max}$ and the ratio of A_1 to A_2 defines the maximum length $\bar{z}_{max}$ of the bridging zone with the following limits on their values: $\gamma \geq 0$; $A_1 = \sigma_{br\,max}$; $0 \leq A_1 \leq \sigma_m$ (σ_m is the matrix strength); $-A_1/A_2 = \bar{z}_{max}$, $0 \leq -A_1/A_2 \leq a - a_0$. The parametric form of the bridging tractions is introduced in the FE model as a user-defined pressure distribution applied to the portion of the delamination surface between the current crack tip and the pre-crack tip. By minimizing the error norm (least squares function $F(\boldsymbol{\alpha})$) that describes the discrepancies between the simulated strains $\tilde{\varepsilon}_{\bar{z}}(\bar{z}, \boldsymbol{\alpha})$ and measured strains $\varepsilon_{\bar{z}}(\bar{z})$:

$$F(\boldsymbol{\alpha}) = \frac{1}{2}\left\| \mathbf{f}(\bar{z}, \boldsymbol{\alpha}) \right\|^2 \text{ with } \mathbf{f}(\bar{z}, \boldsymbol{\alpha}) = \frac{\tilde{\varepsilon}_{\bar{z}}(\bar{z}, \boldsymbol{\alpha}) - \varepsilon_{\bar{z}}(\bar{z})}{\left\langle \varepsilon_{\bar{z}}(\bar{z}) \right\rangle} \quad (5)$$

one can identify the parameters in (4). Further description of this identification technique can be found in [5,7].

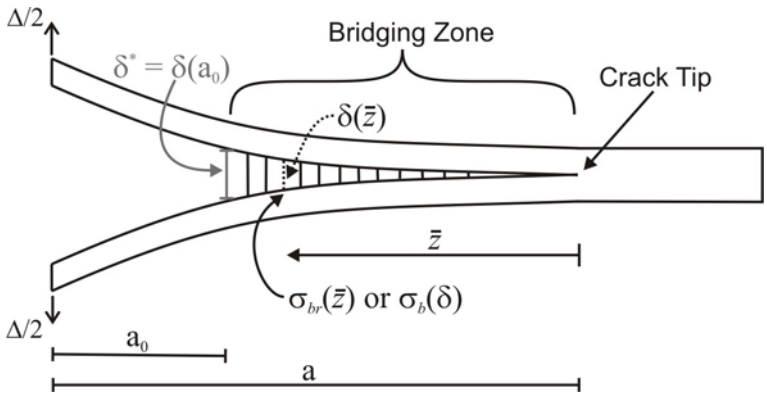

Figure 3: Schematic of DCB specimen with fibre bridging across the delamination crack where a_0 is the pre-crack length; a is the current crack length; δ is the COD; Δ is the applied displacement; $\bar{z}$ is the distance from the crack tip.

4.2 Determination of bridging law using J-integral approach

To define a bridging law, consider the schematic in Figure 3. The bridging fibres are shown by lines crossing the crack plane. These fibres can be represented by position-dependent, equivalent bridging stresses:

$$\sigma_b = \sigma_b(\delta) \quad (6)$$

This function is assumed to be identical for every location along the bridging zone [8]. It is also assumed that the bridging stresses vanish when $\delta = \delta_f$ (δ_f is the maximum separation limit), so that $\sigma_b(\delta_f) = 0$. To evaluate the distribution of the fibre bridging stresses, researchers use the J-integral to represent the ERR G_I, as both are equivalent for an elastic material [2,4,8]. Thus, the following equation represents the J-integral

when it is evaluated along a path containing the crack face in the bridged zone and the crack tip:

$$G_I = J_1 = \int_0^{\delta^*} \sigma_b(\delta) d\delta + G_i \qquad (7)$$

where G_I is the total mode I ERR and $G_i = G_{IC}$ is the mode I ERR required to initiate growth at the crack tip. The integral in (7) represents the energy G_b dissipated in the crack bridging zone, which starts at $\delta = 0$ and ends at the pre-crack tip where $\delta(a_0) = \delta^*$. To experimentally determine the bridging stress distribution, one may differentiate (7) with respect to δ^*:

$$\frac{dG_I}{d\delta^*} = \sigma_b(\delta^*) \qquad (8)$$

In this work, values of G_I are obtained using (1). The method for acquiring δ^* (Figure 3) is based on digital image correlation measurements of points drawn on the correction fluid at the pre-crack tip (Sec. 2). One consequence of this procedure is that the measurements of δ^* are taken during the applied displacement ramp and therefore do not correspond to the equilibrium state achieved during the displacement hold used in sec. 4.1. This implies that the corresponding bridging law can be used to model crack growth and loading pin forces during the ramp opening portion of the tests (subsequently referred to as the "non-equilibrium" state). To produce a bridging law that describes an equilibrium hold situation, it is assumed that the $G_I - \delta^*$ relationship is similar to that of the non-equilibrium curve [7].

4.3 Comparison of Bridging Laws

To compare the J-integral bridging laws with the bridging behaviour found using the FBG method, one must convert the $\bar{z}$ variable into δ. This is accomplished by extracting $\delta(\bar{z})$ from the FE model. A comparison of the bridging laws is found in Figure 4 [7].

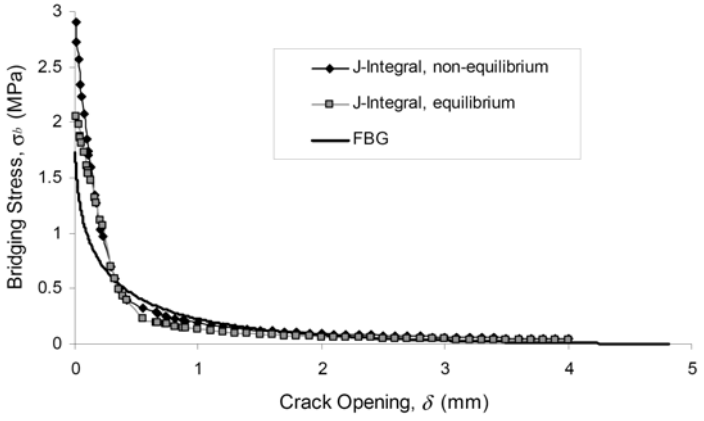

Figure 4: Comparison of bridging laws determined using the J-integral for both equilibrium and non-equilibrium cases, and using the FBG-inverse identification technique [7].

By comparing the corresponding G_b values due to bridging one notes that the bridging laws are similar when it is assumed that δ_f = 4mm for the J-integral method : J-integral equilibrium, G_b =790 J/m^2; FBG-inverse method (for a = 108 mm, in Figure 3); G_b =750 J/m^2; J-integral non-equilibrium, G_b = 940 J/m^2. Although the form of the non-equilibrium law does not seem significantly different from the other two cases (comparing shape and maximum stress, Figure 4), the total area under the curve is sufficient to differentiate it from the other two bridging laws.

5. NUMERICAL MODELING

Fibre bridging along the delamination is modelled in ABAQUS® using a single layer of zero thickness cohesive elements (COH2D4) along the delamination plane (see insert in Figure 5). Cohesive element behaviour of this type is well explained in the literature [3,6]. In the case of mode I delamination, these elements are defined by their "traction-separation" response, meaning that the stress an element incurs as it opens along the crack front depends on the local crack opening displacement δ as it is shown in the Traditional Cohesive Zone illustrated in Figure 5.

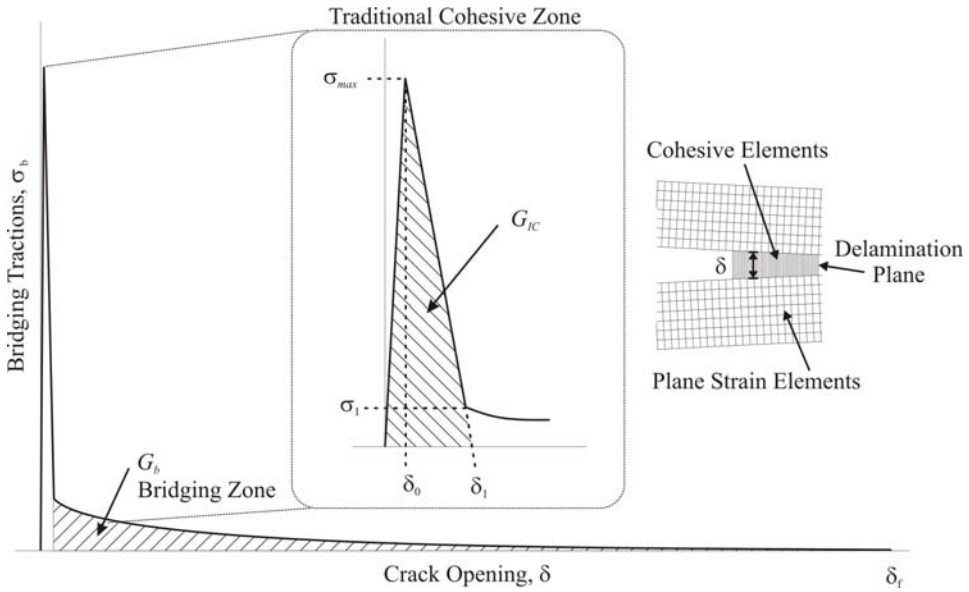

Figure 5: Definition of the constitutive behaviour of a cohesive element with fibre bridging. Insert shows implementation of cohesive element in the case of mode I delamination opening.

Before any damage, elements follow a linear-elastic traction-separation behaviour defined by the stiffness $K_p = \sigma_{max} / \delta_0$ (see Figure 5). Before the maximum stress level $\sigma_b(\delta_0) = \sigma_{max}$, the damage parameter D is zero. After the maximum point, D evolves according to a softening model, which may be linear, exponential or user-defined. In general, the damage increases from 0 to 1 corresponding to $\delta = \delta_0$ and $\delta = \delta_1$ respectively, and the material secant stiffness $(1-D)K_p$ decreases until a pre-defined maximum value of opening displacement δ_1 is achieved. At D = 1 the cohesive elements carry no load.

Due to large-scale fibre bridging, it is assumed that the composite first undergoes decohesion followed by fibre bridging. Thus we use a three-part cohesive model as illustrated in Figure 5 [2]. The area under the triangle in the first part of the separation (insert in Figure 5) represents $G_I = G_{IC} = \sigma_{max}\delta_1/2$. The third part of the cohesive element law describes the bridging zone, and is defined on the basis of the bridging stress functions $\sigma_b(\delta)$ from the results of the previous sections. The area under the bridging zone portion of the curve ($\delta_1 \leq \delta \leq \delta_f$) is defined by the separation ERR G_b.

The general model configuration considered here follows the schematic in Figure 3. As in the experiments, a displacement Δ is applied to open the delamination and the crack length a is allowed to develop freely as the cohesive elements separate and break. Non-linear geometry is accounted for; however, to reduce calculation costs, the proposed FE model assumes plane strain conditions along the width of the specimen. Consequently, the model is considered to be representative of the centre of the specimen. The composite beam is simulated by 32 000 linear, plane strain elements with the same mechanical properties that were used in the inverse identification method [5, 7]. Cohesive elements (0.05mm wide) are inserted along the crack plane as shown in Figure 5, starting at the pre-crack tip position, $a_0 = 63$ mm, and continuing to the end of the specimen. This layer of elements is fixed to the plane strain elements using tie constraints. The input parameters for the cohesive element are $G_{IC} = 150$ J/m^2; $\sigma_{max} = 36$ MPa; $K_p = 10000$ Nmm^{-3}. The G_{IC} is taken within the range of the experimentally measured values and K_p is equal to the transverse modulus E_{22} divided by the constitutive element thickness of one. The σ_{max} is assumed to be about 40% of the matrix yield strength or 36 MPa on the suggestion of reference [3] with respect to convergence issues. With high σ_{max} values, convergence becomes difficult, thus this model relies on G_{IC}, instead of the exact value of σ_{max}. It must be noted, however, that G_{IC} and σ_{max} will influence the progression of cracking, and they should not be dismissed when considering the potential errors of this method. In addition to the lowering of the maximum stress, a small value of viscous regularization, $1 \cdot 10^{-5}$ is required to help the convergence of the model. In preliminary tests, this value does not noticeably affect the force-displacement results; however, care must always be taken in the choice of this parameter. The third part of the bridging law is described using the bridging stress distributions determined using both the J-integral and the FBG-inverse identification methods.

To investigate the impact of the different bridging laws on delamination behaviour, as predicted by the cohesive model, two different simulations are reported herein: (1) In a first step, the non-equilibrium law determined using the J-integral approach is implemented with $\delta_f = 4$ mm and $\Delta = 25.26$ mm. In a second step, the displacement is held constant while using the equilibrium law to simulate the actual ramp-hold procedure of the experiment: (2) The bridging law determined using the FBG-inverse identification technique is implemented for an applied $\Delta = 25.26$ mm. This law represents the equilibrium (hold) behaviour of the delamination. Output from the cohesive models is displayed in terms of the force-displacement P-Δ response of the DCB specimen. These two cases are shown in Figure 6 [7]. Case 1, $\delta_f = 4$ mm,

simulates an actual test case, where the first step follows the displacement ramp and the second step represents the time when the specimen is held open at a fixed displacement (Δ = 25.3 mm). By applying the non-equilibrium cohesive law in the second step, the delamination crack continues to grow, (more cohesive elements rupture) so that the force decreases for a fixed displacement. This result agrees well with the experimentally observed decrease in force. Case 2 illustrates the behaviour of the specimen based on the bridging law obtained from the FBG-inverse identification method. Its results are comparable to the lowest force values obtained during the displacement holds (Δ = 14.5, 19.9, and 25.3 mm) since its FBG measurements were taken during such displacement holds. During the initial loading, this model follows the same linear response as in case 1, but once the cohesive element softening behaviour starts to influence the model, the calculated forces follow a low curve that touches the force values obtained during the fixed-displacement holds. At the hold when Δ = 25.3 mm the forces calculated in cases 1 and 2 are comparable.

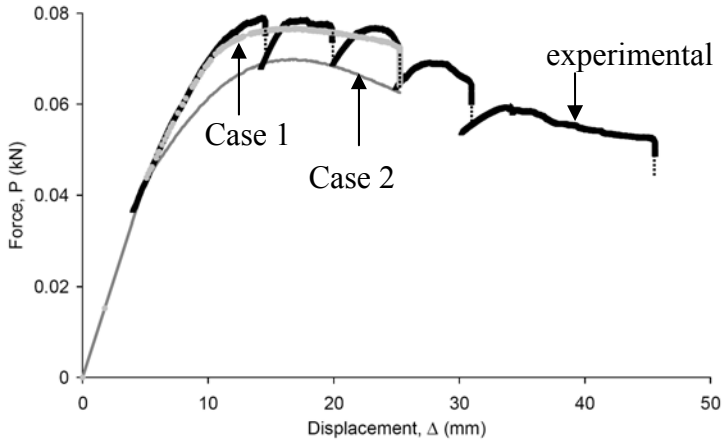

Figure 6: Force displacement response compared with results from cohesive elements. Note the drop in the case 1 load towards that of case 2 at Δ = 25.3 mm.

6. CONCLUSIONS

In this work two techniques are used to determine bridging stress distributions in mode I delamination of uniaxial carbon fibre-reinforced polymer composite. While both methods produce similar bridging laws, the J-integral approach requires a choice of the δ_f value. Regardless of the technique used to determine bridging laws, accurate crack tip position, and the resulting local strain distribution are difficult to simulate, due to the need to assume an initial stiffness and maximum stress before damage is incurred. Note also that the choice of appropriate values in the traditional cohesive zone is dictated not only by G_{IC}, but also by the need for numerical convergence. The results of this work demonstrate that distributed strain data from embedded long FBG sensors and inverse numerical identification provide an independent semi-experimental means for determining bridging laws that can be used to characterise delamination behaviour in polymer composites.

ACKNOWLEDGEMENTS

The authors wish to acknowledge the financial support from the Swiss National Science Foundation under grant 2000-068279 and Cytec industries for providing the pre-preg.

REFERENCES

[1] Tay T.E., 'Characterisation and analysis of delamination fracture in composites: An overview of developments from 1990 to 2001', *Applied Mechanics Reviews* 2003;56:1-31.

[2] Tamuzs V., Tarasovs S., Vilks U., 'Progressive delamination and fiber bridging modeling in double cantilever beam composite specimens', *Engineering Fracture Mechanics*, 2001;68:513-525.

[3] Camanho P.P., Dávila C.G., Ambur D.R., 'Numerical simulation of delamination growth in composite materials', NASA Langley Research Center, Hampton, NASA/TP-2001-211041, 2001.

[4] Sorensen B.F., Jacobsen T.K., 'Determination of cohesive laws by the J integral Approach', *Engineering Fracture Mechanics*, 2003;70:1841-1858.

[5] Sorensen L., Botsis J., Gmür T., Cugnoni J., 'Delamination detection and characterisation of bridging tractions using long FBG optical sensors', *Composites Part A,* 2007;38:2087-2096.

[6] de Borst R., Remmers J.J.C., 'Computational modeling of delamination', *Composites Science and Technology*, 2006;66:713-722.

[7] Sorensen L., Botsis J., Gmür T., Hunbert, L., 'Bridging tractions in mode I delamination: Measurements and simulations', *Composites Science and Technology*, doi:10.1016/j.compscitech.2007.08.024, to appear.

[8] Suo Z., Bao G., Fan B., 'Delamination R-curve phenomena due to damage', *Journal of the Mechanics and Physics of Solids*, 1992;40:1-16.

[9] Takeda S., Okabe Y., Takeda N., 'Delamination detection in CFRP laminates with embedded small-diameter fiber Bragg grating sensors', *Composites Part A*, 2002; 33:971-980.

[10] Ling, H-Y., Lau K-T., Cheng , Su Z., 'Mode II fracture behaviour monitoring for composite laminates using embedded fibre Bragg grating sensors' *Composites Structures*, 2006;76:88–93.

[11] Takeda N., Okabe Y., Tsuji R., Takeda S.I., 'Application of chirped fiber Bragg grating sensors for damage identification in composites', Smart structures and materials 2002: Smart sensor technology and measurement systems Proc SPIE, Inaudi D, Udd E, editors. vol. 4694. San Diego; SPIE, 2002:106-117.

[12] Giaccari P., Dunkel G.R., Humbert L., Botsis J., Limberger H.G., Salathé R.P., 'On a direct determination of non-uniform internal strain fields using fibre Bragg gratings', *Smart Materials and Structures*, 2005;14:127-136.

[13] Hellan K., Introduction to Fracture Mechanics, McGraw-Hill, 1984

[14] Davies P., Benzeggagh M. L., de Charentenay F. X., 'Delamination behavior of carbon fiber reinforced PPS', 32nd International SAMPE Symposium & Exhibition: Advanced Materials Technology '87, Covina, CA, USA, 1987:134-146.

[15] Ma C.C.M, O'Connor J.E., Lou A.Y., 'Polyphenylene sulfide high performance composites'. *SAMPE Quarterly*, 1984;15:12-17.

[16] O'Connor J.E., Lou A.Y., Beever W.H., 'Polyphenylene sulfide – a thermoplastic polymer matrix for high performance composites', ICCM-5, San Diego, 1985: 963-970.